Journal Pre-proofs

Article

Tactile tribotronic reconfigurable p-n junctions for artificial synapses

Mengmeng Jia, Pengwen Guo, Wei Wang, Aifang Yu, Yufei Zhang, Zhong Lin Wang, Junyi Zhai

PII: S2095-9273(21)00766-0
DOI: https://doi.org/10.1016/j.scib.2021.12.014
Reference: SCIB 1653

To appear in: *Science Bulletin*

Received Date: 5 October 2021
Revised Date: 13 November 2021
Accepted Date: 5 December 2021

Please cite this article as: M. Jia, P. Guo, W. Wang, A. Yu, Y. Zhang, Z.L. Wang, J. Zhai, Tactile tribotronic reconfigurable p-n junctions for artificial synapses, *Science Bulletin* (2021), doi: https://doi.org/10.1016/j.scib.2021.12.014

This is a PDF file of an article that has undergone enhancements after acceptance, such as the addition of a cover page and metadata, and formatting for readability, but it is not yet the definitive version of record. This version will undergo additional copyediting, typesetting and review before it is published in its final form, but we are providing this version to give early visibility of the article. Please note that, during the production process, errors may be discovered which could affect the content, and all legal disclaimers that apply to the journal pertain.

© 2021 Science China Press. Published by Elsevier B.V. and Science China Press. All rights reserved.

Article

Received 5 October 2021

Received in revised form 13 November 2021

Accepted 5 December 2021

Tactile tribotronic reconfigurable p-n junctions for artificial synapses

Mengmeng Jia [a,b,1], *Pengwen Guo* [a,b,1], *Wei Wang* [a,b], *Aifang Yu* [a,b,c], *Yufei Zhang* [a,b], *Zhong Lin Wang* [a,b,d,*], *Junyi Zhai* [a,b,c,*]

a. CAS Center for Excellence in Nanoscience, Beijing Key Laboratory of Micro-nano Energy and Sensor, Beijing Institute of Nanoenergy and Nanosystems, Chinese Academy of Sciences, Beijing 100083, China

b. School of Nanoscience and Technology, University of Chinese Academy of Sciences, Beijing 100049, China

c. Center on Nanoenergy Research, School of Physical Science and Technology, Guangxi University, Nanning 530004, China

d. School of Materials Science and Engineering, Georgia Institute of Technology, Atlanta, GA 30332, USA

***Corresponding Authors.** zlwang@gatech.edu (Z. L. Wang); jyzhai@binn.cas.cn (J. Zhai)

[1] These authors contributed equally to this work.

Abstract

The emulation of biological synapses with learning and memory functions and versatile plasticity is significantly promising for neuromorphic computing systems. Here, a robust and continuously adjustable mechanoplastic semifloating-gate transistor is demonstrated based on an integrated graphene/hexagonal boron nitride/tungsten diselenide van der Waals heterostructure and a triboelectric nanogenerator (TENG). The working states (p-n junction or n^+-n junction) can be manipulated and switched under the sophisticated modulation of triboelectric potential derived from mechanical actions, which is attributed to carriers trapping and detrapping in the graphene layer. Furthermore, a reconfigurable artificial synapse is constructed based on such mechanoplastic transistor that can simulate typical synaptic

Journal Pre-proofs

plasticity and implement dynamic control correlations in each response mode by further designing the amplitude and duration. The artificial synapse can work with ultra-low energy consumption at 74.2 fJ per synaptic event and the extended synaptic weights. Under the synergetic effect of the semifloating gate, the synaptic device can enable successive mechanical facilitation/depression, short-/long-term plasticity and learning-experience behavior, exhibiting the mechanical behavior derived synaptic plasticity. Such reconfigurable and mechanoplastic features provide an insight into the applications of energy-efficient and real-time interactive neuromodulation in the future artificial intelligent system beyond von Neumann architecture.

Keywords

Reconfigurable p-n junction, Semifloating-gate transistor, Triboelectric potential, Artificial synapses, Synaptic plasticity

1. Introduction

Conventional von Neumann computing architecture suffers from poor fault tolerance, complex algorithms, low energy efficiency, and incompatible performance [1] dealing with a considerable amount of information due to physically separated processor and memory blocks, which inevitably face the problem of incompatible performance and huge energy consumption [2, 3]. In contrast, a human brain is considered as the most robust and efficient computing system, consisting of highly interconnected and large-scale parallel neuronal networks. The network is composed of a huge number of neurons ($\approx 10^{12}$) and synapses ($\approx 10^{15}$) that underlie thought, emotion and behavior [4]. As a functional link of two neighboring neurons, biological synapses can simultaneously perform the functions of transmitting and processing information by releasing neurotransmitters and strengthening or weakening the synaptic weight, which is the basis of learning and computing [4, 5]. Aiming to perform parallel, distributed, and event-driven-computation information processing, the recent emerging field of neuromorphic electronics relied on constructed artificial neural networks and synapses provides a promising way to endow electronic devices with biological intelligence beyond the von Neumann bottleneck [6–8]. As a key component of conducting the information processing, artificial synaptic devices have attracted widespread attention on

Journal Pre-proofs

mimicking neural and synaptic functions based on two- and three-terminal memory devices. Two-terminal memory devices, such as resistive random access memory (RRAM) possess the advantages of high scaling ability and low energy consumption [9, 10]. At the same time, there are still obvious limitations to achieve nondestructive synaptic weight update and highly efficient information processing due to the same terminal for learning and processing. Three-terminal transistors [11–13], by contrast, are capable of effectively simulating the parallel signal processing because of separated read (drain) and write (gate) terminals, which offers more feasibility and flexibility for the sophisticated requirements. By applying a fourth terminal as a real-time monitor, synaptic transistor can even achieve avoidance tendency of negative stimuli and lasting memory of positive emotion, thereby emulating automatic emotion regulation [14]. It is also necessary to exploit the synaptic transistor to more complex neuromorphic hardware systems with high recognition accuracy and computing efficiency [15–17]. Furthermore, tactile perceptual learning systems research has been the latest frontier in sensory neuroscience because tactile information is vital for neuromorphic computing. The synaptic device can recognize spatiotemporal input and implement complex neuron functions by integrating self-powered sensors with transistors. Thus, a proposed self-powered artificial synapse offers a favorable option for achieving interactive sensation recognition and low energy consumption in neuromorphic systems.

Triboelectric nanogenerator (TENG) based on the ubiquitous effect of contact electrification has been proposed by Wang since 2012 [18, 19], which offers a versatile way to convert a variety of ambient mechanical energy into electricity for micro/nano power source [20, 21], self-powered active sensors [22, 23], and blue energy [24, 25]. Particularly, the carrier transport properties could be modulated under the imposition of mechanical stimuli by coupling triboelectricity and semiconductor device, which implements the direct interaction between external environment and electronics (e.g., tribotronics) [26]. Previous studies on constructing p-n junctions mainly focus on thickness modulation [27, 28], chemical doping [29], ion implantation [30], electrostatic doping [31–33], and ferroelectric polarization [34, 35] to spatially control the carriers. Atomic/ionic doping and surface modification cause permanent changes of impurities and defect states to obstruct its electrical properties. Electrostatic doping p-n junctions based on local split gates can effectively control the carrier

type in different channel regions, but defining p-n configuration requires high and continuous voltage due to two local gates, that is, the device is volatile. Although ferroelectric polarization control allows for patterning the domain with arbitrary shape and size in a nonvolatile manner, it requires a complex scanning probe technology that obviously hinders its large-scale integration with complementary metal oxide semiconductor techniques and limits operation efficiency. Thus, constructing tunable functional devices in a programmable and mechanical manner, which takes advantage of nonvolatile and low-power properties, is significantly promising for multifunctional and versatile devices.

Herein, we demonstrate a reconfigurable tribotronic nonvolatile device to mimic the intrinsic biological synapse characteristics under the synergetic effect of triboelectric potential and semifloating-gate layer. The bioinspired artificial synapse is based on a stacked heterostructure of graphene/hexagonal boron nitride (h-BN)/tungsten diselenide (WSe_2) semifloating-gate field-effect transistor gated by triboelectric potential from an integrated TENG component. The working states (p-n junction or n^+-n junction) can be flexibly manipulated and switched, exhibiting a good rectifying behavior as the p-n state (rectification ratio of 2.96×10^3). Our tribotronic memory device exhibits a high on/off ratio (~10^6), good retention and endurance characteristics. Moreover, it can function as an artificial synapse. Analogy to biological synapses, the TENG served as a mechanoreceptor is connected to postsynaptic transistor gate, through which converts mechanical pulse into presynaptic voltage spike and then transmits them for processing. Here, the synaptic weights could be effectively modulated by mechanical inputs. The channel conductance could exhibit a nonvolatile and continuously changing behavior by manipulating the type and density of carriers in the semifloating layer, which underlies synaptic plasticity including short-/long-term plasticity. Our artificial synapse also has the prospective benefit of a substantial decrease in energy consumption, to the femtojoule level (74.2 fJ/spike). More importantly, the synapse can respond to the amplitude and duration of external motions under the sophisticated modulation of mechanical signals applied to the gate terminal. The demonstrated artificial synapses broaden the application prospects in the mechanical behavior derived artificial neuromorphic network requiring real-time interaction and low energy consumption.

2. Experimental

2.1. Device fabrication

The heterostructures were fabricated with an all-dry transfer method. The graphene, h-BN, and WSe_2 nanoflakes were all purchased from Nanjing MKNANO Tech. Co., Ltd. First, a few-layer graphene flake was mechanically exfoliated from highly oriented pyrolytic graphite (HOPG) onto a SiO_2 (285 nm)/Si substrate. Afterward, h-BN and WSe_2 flakes were produced onto the transparent polydimethylsiloxane (PDMS) stamp by using scotch tape and sequentially aligned and transferred onto the bottom graphene flake with the help of an optical microscope (OM) to form vertically stacked WSe_2/h-BN/graphene heterostructure. Finally, source and drain electrodes were patterned by standard electron beam lithography and then Cr/Au (10/50 nm) electrodes were deposited by thermal evaporation. The deposition rates of Cr and Au are 0.1 and 0.3 Å/s respectively. The integrated TENG was composed of one friction layer (50 μm thick FEP film against Cu electrode) supported by an acrylic sheet and the other Cu friction layer. The size of TENG component was 12 mm× 12 mm, as shown in Fig. S1a (online).

2.2. Characterizations

The morphology of fabricated devices was obtained by OM (Olympus BX51M) and scanning electron microscopy (SEM, Nova NanoSEM 450). The corresponding thickness of flakes was characterized by Raman spectroscopy (HORIBA/LabRAM, 532 nm excitation laser) and atomic force microscopy (AFM, Asylum Research MFP-3D). Electrical properties were conducted by a probe station equipped with a semiconductor parameter analyzer (Agilent B1500A) in the ambient environment. The displacement of TENG was controlled by a linear motor with the velocity of 20 mm/s and the acceleration of 50 mm/s^2, whereas the TENG characterizations were performed synchronously using a Keithley 6514 system electrometer.

3. Results and discussion

3.1. Design of mechanoplastic artificial synapse

Our mechanical stimuli-driven artificial synapse mimics the principles of the human tactile sensory system. The schematic in Fig. 1a illustrates the human tactile reception system and the release of neurotransmitters that occurred in synapses, respectively. Mechanoreceptors such as Merkel cell-neurite complexes could respond to external stimuli

and generate touch-evoked electrical impulses, thus enabling the tactile information transmission to the brain. The complexes are called synapse-like connections between Merkel cells and afferents [36, 37]. Synapses are the functional connections between two adjacent neurons (presynaptic and postsynaptic neurons), which are elements of neural information transmission via neurotransmitters. The release of neurotransmitters leads to the excitatory postsynaptic current (EPSC) or the inhibitory postsynaptic current (IPSC). Inspired by the human tactile sensory, an intelligent artificial sensory nerve incorporated with the feature of mechanoreceptors can receive external mechanical stimulus and preprocess tactile information. As schematically illustrated in Fig. 1b, we demonstrate a triboelectric-potential-activated artificial synapse that converts mechanical energy to electricity to emulate intelligent functions, endowing it with synaptic characteristics. The device is composed of a van der Waals heterostructure of graphene/h-BN/WSe_2 and an integrated TENG in contact-separation mode. A schematic illustration of the tribotronic transistor is shown in Fig. S1 (online). Here, only half of the WSe_2 conducting channel is aligned vertically over the graphene flake to form semifloating-gate field-effect transistor (SFG-FET) architecture. The bottom graphene layer acts as the floating gate, the Si is the control gate, and the h-BN and the SiO_2 serve as tunneling barrier and blocking dielectrics, respectively. The TENG component comprises of Cu/fluorinated ethylene propylene (FEP)/Cu with one fixed Cu friction layer coupled to the transistor gate and the other mobile friction layer (FEP/Cu). The complete fabrication process is described in the Experimental section and Fig. S2 (online) in detail. The triboelectric potential is applied to the gate terminal from mechanical stimuli, described as the displacement (D) between two triboelectrification layers. Then, the intrinsic symmetrical current of the transistor is modulated into a diode-like current. Similar to tactile information in the neural network, the external displacement information (the amplitude and duration time of D) can trigger the triboelectric potential, which is regarded as a presynaptic action potential to gate the channel. The corresponding drain current and the produced current change are usually recorded as the postsynaptic current (PSC) and synaptic weight, respectively. Fig. 1c shows a false-color SEM image of the fabricated devices. Fig. 1d displays AFM image of the stacked heterostructure and the thicknesses of graphene, h-BN, and WSe_2 along the solid lines are determined to be 4.1, 13.4, and 13.5 nm from height

profiles (Fig. S3 online), respectively. The heterostructure components were further characterized by Raman spectroscopy. As shown in Fig. 1e, different typical Raman peaks of graphene (G peak at 1582 cm^{-1} and 2D peak at 2720 cm^{-1}), h-BN (E_{2g} peak at 1365 cm^{-1}), and WSe_2 (six peaks at 250, 260, 308, 360, 374, and 396 cm^{-1}) [38] flakes are observed in the corresponding spectrum.

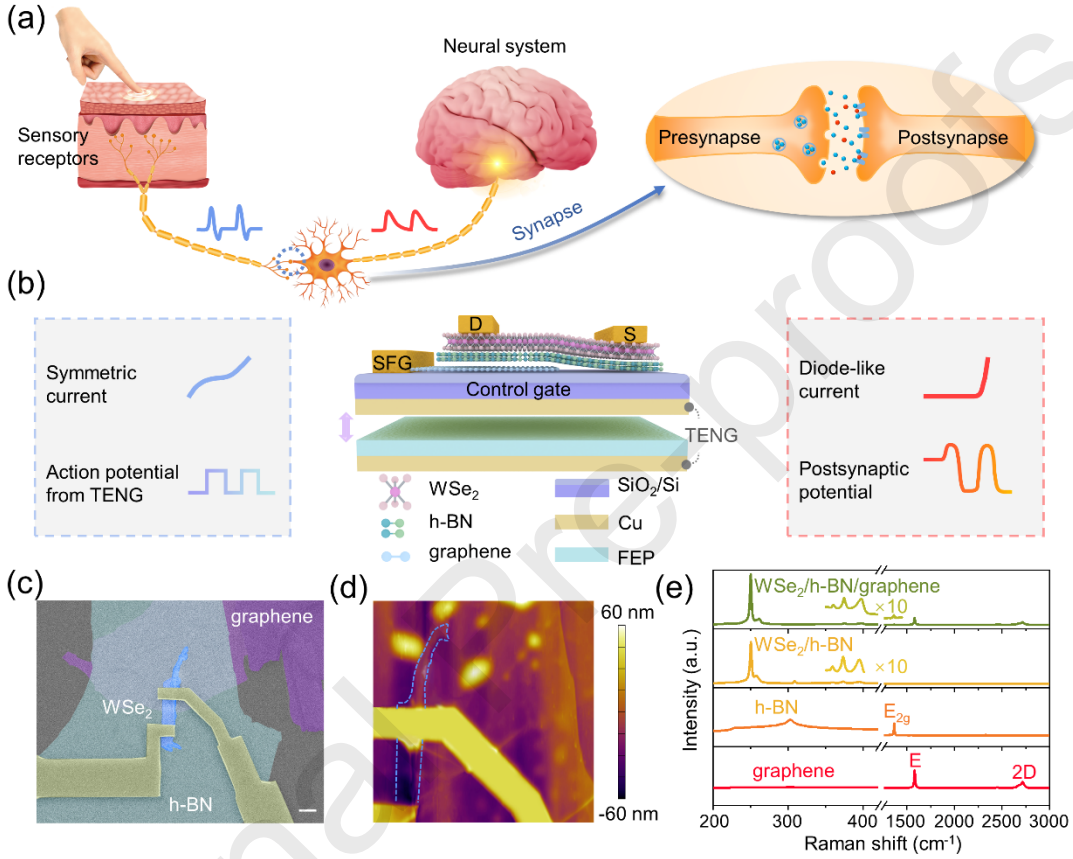

Fig. 1. (Color online) Schematic of the human tactile sensory system and TENG-driven artificial neuromorphic device. (a) Schematic illustration of the biological tactile afferent nerve system and its synapse (right part). Action potential combines through synapses and contributes to human brain information processing. (b) The artificial tactile perceptual neuron, comprising of a graphene/h-BN/WSe_2 semifloating-gate synaptic transistor and an integrated TENG (SFG: semifloating gate, D: drain electrode, S: source electrode). Diode-like current rectifying behavior activated by triboelectric potential is observed, distinguished from its symmetrical current. Action potential is generated by TENG component and leads to a postsynaptic potential change. (c) False-colored SEM image of a typical fabricated device. Scale bar, 5 μm. (d) AFM surface morphology of the heterostructure. (e) Raman spectra of graphene, h-BN, WSe_2, and their heterostructure regions excited by 532 nm laser.

3.2. Operating mechanism of the mechanoplastic p-n junctions

To explore the operation mechanism of mechanoplastic SFG-FET device, we firstly investigate the electrical behaviors and formation mechanism of p-n junction state under the action of mechanical displacement. It is worth noting that the initial output characteristic curve (I_d-V_{ds}, I_d: the drain current, V_{ds}: the drain bias voltage) (Fig. 2a) is almost symmetric and the current depends linearly on the bias voltage at low voltages, as shown in the inset of Fig. 2a. With the separation displacement D = 15 μm (duration time of 1 s) of TENG coupled to the transistor gate, a lateral p-n junction can be formed along the WSe_2. The channel is nonvolatile and programmable, exhibiting an evident rectifying behavior with a rectification ratio of 2.96×10^3 (Fig. 2b). By fitting the I_d-V_{ds} curve with the Shockley equation, an ideal factor of 1.98 and a series resistance of 6.74 MΩ are obtained, which indicates that the transport is most likely dominated by recombination process rather than diffusion (Fig. S4 online). Furthermore, the rectification ratio can be modulated by increasing displacement from 12 to 18 μm with 1 s duration. A remarkably improved rectifying characteristic can be obtained with an increasing displacement, as illustrated in Fig. 2c. However, when the graphene is electrically grounded, the current will immediately return back to its initial value before applying mechanical pulse, as under such situation these trapped charges would flow away (Fig. S5 online). Fig. 2d–f elucidate the charge transfer in the p-n junction formation process and the correlative energy band diagrams. In the original state, the equivalent triboelectric potential is preset to be 0 V with a certain position of D_0 by short-circuit connection between the bottom Cu/FEP layer and the top Cu electrode, equivalent to no voltage dropped on the transistor gate. Under this circumstance, there is no effect on the Fermi level of the graphene/h-BN/WSe_2 heterostructure (Fig. 2d). The positive or negative relative displacement means that the mobile FEP/Cu layer and Cu friction layer separate or approach to each other from the preset position (D_0, defined as 0). And the increased and decreased displacements from the position of D_0 are defined as the positive (+D) and negative (−D) relative displacement accordingly. The working mechanism of the transistor modulated by mechanical displacements is illustrated in Fig. S6 (online). When the two friction layers start to separate (+D), more positive charges are free from bounding in the attached Cu

electrode, which induces an equivalent positive voltage ($+V_{TENG}$) applied to the Si gate. Hence, a high density of electrons accumulation in the WSe_2 flake and the downward energy band would be induced, leading to a positive built-in electric field between the graphene and WSe_2 layer. The electrons in the channel are prompted to tunnel through the h-BN dielectric via Fowler-Nordheim mechanism to accumulate in the semifloating layer simultaneously. Due to the potential barrier, the h-BN dielectric layer can hold these trapped electrons even after removing the induced $+V_{TENG}$. The electrons synchronously produce a negative electric field to deplete electrons in the half of WSe_2 over the graphene, resulting in p-type polarity. WSe_2 is intrinsically n-doped, and thus the rest of the channel presents n-type polarity [39]. At this state, two opposite conductive polarities occur along the WSe_2 channel and the resultant p-n homojunction is formed, which exhibits clear rectifying behavior. On the contrary, with the distance between the Cu electrode and Cu/FEP layer further decreased compared to the initial state ($-D$), $-V_{TENG}$ can be induced and coupled to gate the WSe_2 channel. The stored holes in the graphene will produce mirror-imaged electrons in the WSe_2 over the graphene, which enables the device to behave as n^+-n junction. The electrical transport characterization across the WSe_2 with different D pulses of 1 s duration and corresponding mechanism are illustrated in Fig. S7 (online). However, in the floating-gate transistor, the channel is completely within the range of the floating gate. Thus, the channel can only exhibit low- or high-current state, instead of two polarities at the same time.

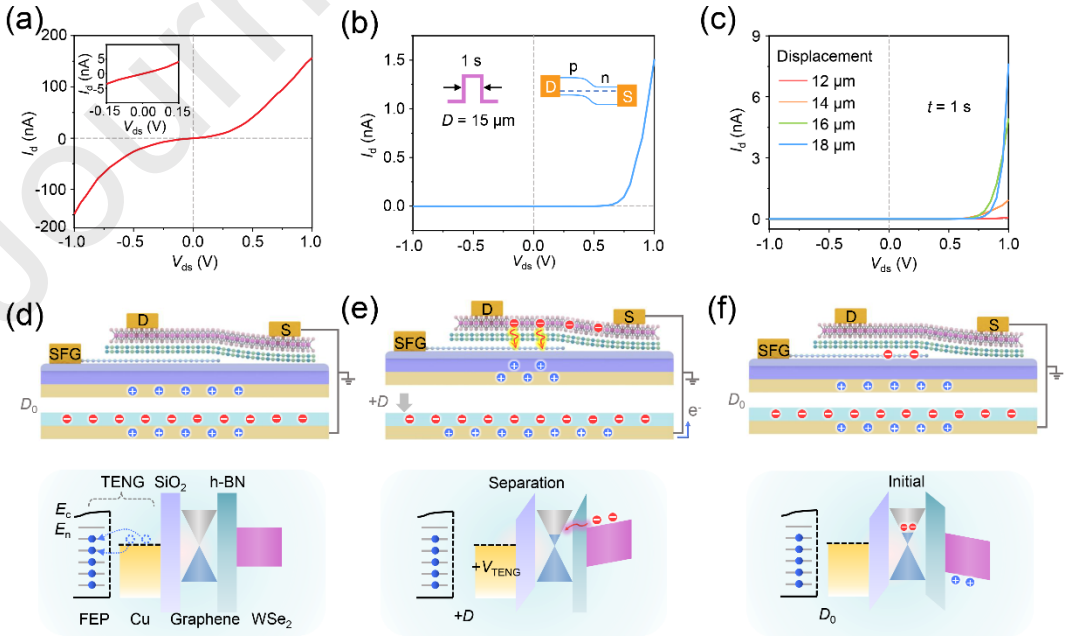

Fig. 2. (Color online) Nonvolatile WSe_2 p-n junction under the modulation of mechanical displacement pulses and corresponding working mechanism. (a) I_d-V_{ds} curve of the SFG-FET device without applied displacement pulse. Inset: the output curve exhibits nearly symmetric current with a small sweep range. (b) I_d-V_{ds} curve across the WSe_2 with the applied D pulse (D = 15 μm, t = 1 s) on the Si. Inset: band diagram of the device at p-n junction state. (c) I_d-V_{ds} curves across the WSe_2 with different D pulses (t = 1 s). D varies from 12 to 18 μm. Schematic illustrations of the working mechanism and the corresponding energy band diagram at (d) original state, (e) charge doping state with a positive relative displacement (+D), and (f) charge doping state after removing the positive relative displacement.

3.3. Characterization of the SFG-FET device

The excellent performance of the SFG-FET device is vital for the subsequent realization of imitating biological synapses, so we measure the electrical properties of the transistor by a probe station in a vacuum chamber. Fig. 3a displays the typical transfer curves with a forward and reverse gate voltage (between −80 and +80 V) and the arrowheads indicate the corresponding Si control gate scanning directions. Different from general full-floating-gate transistors, the SFG device exhibits two distinct hysteresis windows with the V_{ds} fixed at −1 and +1 V originated from trapped charge in the semifloating layer, which is dependent on the bias voltage direction. The observed hysteresis windows can be further developed for memory devices. When the V_{ds} is switched to −1 V, the transfer curve shows a larger hysteresis window than V_{ds} = +1 V. Then, triboelectric potential pulses (or displacement pulses) are often employed as the programming and erasing triggers and V_{TENG} is set to be 0 V at the reading process. Here, we mainly focus on the right window because V_g = 0 V is in this region. The device shows a fairly high erasing/programming current ratio with V_{ds} = −1 V compared with V_{ds} = +1 V. The V_{ds} direction-dependent behavior is attributed to the stored carriers (either electrons or holes) in the floating layer, which play an essential role in the modulation of the spatial contribution of charge along the WSe_2, denoting rectifying behaviors in both p-n and n^+-n junctions. This result indicates the SFG memory could be read in multimode, which depends on not only the direction of the V_{ds}, but also the triboelectric voltage pulse. The SFG-FET exhibits a good reproducibility. The transfer curves of different transistors show two

obvious memory windows. Also, the device exhibits similar rectifying behavior after applying displacement pulses (Fig. S8 online). Meanwhile, excellent reliability performance is an essential requirement for nonvolatile mechanoplastic memory applications. The curves of I_d over time are independently investigated after application of a positive relative displacement (D = +40 μm) and a negative relative displacement (D = −40 μm) for 1 s on the control gate with a forward bias (+1 V) and a reverse bias (−1 V) as shown in Fig. 3b. The drain current can be programmed by applying $+V_{TENG}$ and maintained at the 'off' state in the p-n junction, whereas the $-V_{TENG}$ can implement erasing procedure and the current switches back to the 'on' state in the n^+-n junction. All current states are very stable within 1200 s with a nearly negligible variation. Moreover, the on/off current ratio at V_{ds} = −1 V reaches 10^6, which is much higher than that at V_{ds} = +1 V (≈ 500). Fig. 3c, d show the dynamic performance of periodic TENG-driven programming (1 s) -reading (5 s)-erasing (1 s)-reading (5 s) cycles for V_{ds} = +1 and −1 V. The device could be readily switched between the 'on' state and 'off' state by manipulating an alternate relative displacement pulse for 1 s. Given the superior retention and endurance performances, and reconfigurable nonvolatile doping configurations, the two distinct read modes allow for more flexible operation for emulating biological synapse function, especially learning and memory stimulation.

Journal Pre-proofs

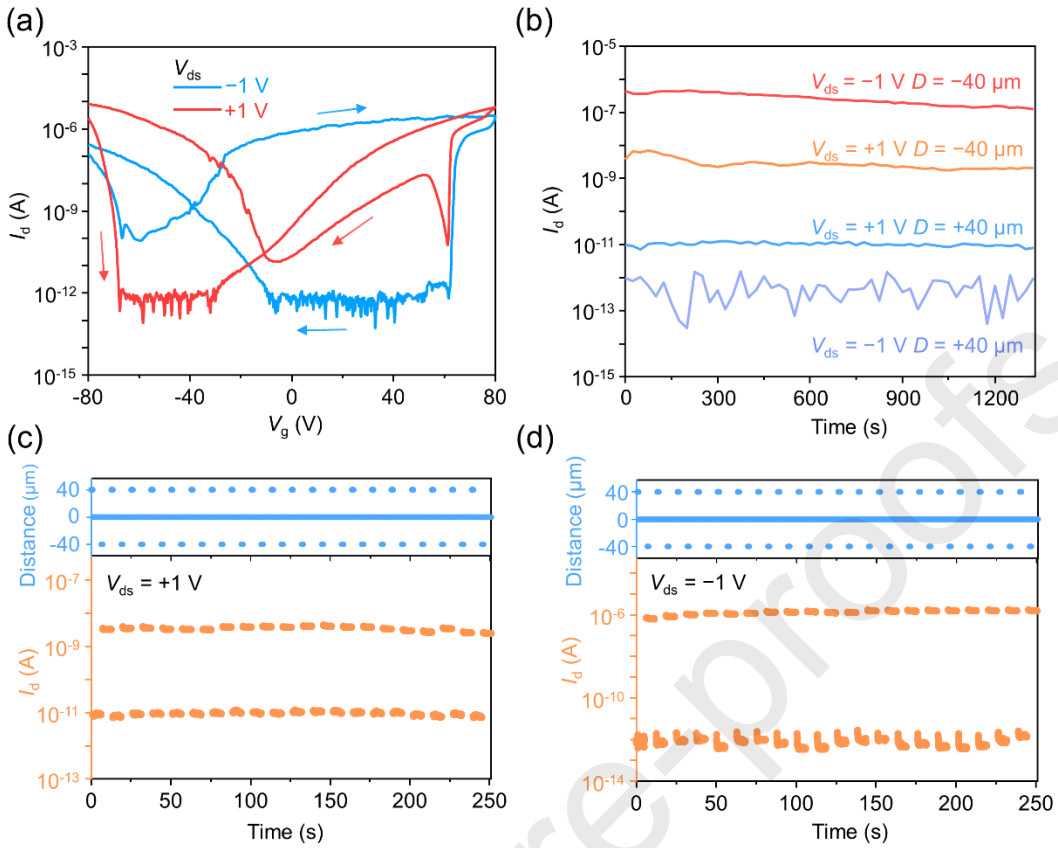

Fig. 3. (Color online) Electrical characterizations of the SFG-FET device for nonvolatile applications. (a) Dual-sweep I_d-V_g transfer curves of the device with V_{ds} = ±1 V. Sweeping directions are indicated by arrowheads. (b) Retention properties at various junction state by applying different D pulses with V_{ds} = ±1 V. The transistor exhibits the 'off' state programmed by positive D pulse and the 'on' state erased by negative D pulse with pulse width of 1 s. (c, d) Endurance performances for 20 cycles of the device. Switching behaviors between the programming states and erasing states based on the periodic alternative displacement (D = ± 40 μm, t = 1 s) with V_{ds} = ±1 V.

3.4. Typical synaptic features of the TENG-driven synaptic transistor

To further testify the feasibility of precise mechanical displacement pulse modulation in our synaptic transistor, we conduct the output characteristics of the integrated TENG. During the separation-contact process, the output voltage shows a periodic and stable variation (from 0 to 62 V) in response to increased displacement with a step size of 2 μm (Fig. S9a online). The transient triboelectric potential related to the separation distance can be found in more

details in Fig. S9b, c (online) and the voltage increases from 0 to 65 V synchronously with the increased displacement from 0 to 30 μm stepped by 2 μm. Similarly, the instantaneous voltage shows a decreased trend (from 0 to −66 V) under the reverse process. In contrast to reported traditional artificial synapses triggered by electrical signals, we utilize the various displacements to modulate consecutively both the EPSC and the IPSC in our artificial synaptic transistors. The successful emulation of synaptic depression and potentiation behaviors under the influence of mechanical displacement (i.e., triboelectric potential) is displayed in Fig. 4, where the triboelectric potential derived from the contact-separation TENG component acts as the input spike to trigger the PSC through the bottom gate. Upon the presynaptic spike (a positive relative distance of 30 μm) with pulse width of 1 s applied in Fig. 4a, a current surge appears instantaneously owing to an equivalent $+V_{TENG}$ coupled to the bottom gate and the intrinsic n-doping property of WSe_2. Subsequently, the IPSC exhibits an immediate and significant decrease after removing the *D* pulse and reaches a very stable level with a slow decay trend, conferring long-term depression (LTD), attributed to the non-volatility of the SFG-FET devices. In this process, the captured electrons induced by $+V_{TENG}$ in the graphene layer could lead to a much lower postsynaptic current even though the displacement is changed back to the initial state. This behavior is quite similar to the inhibitory postsynaptic current caused by a release of inhibitory neurotransmitters. Conversely, a negative relative *D* pulse (−18 μm, 1 s) induces notable postsynaptic current enhancement. The EPSC response begins to plunge sharply and then increases to an order of magnitude above its initial current shown in Fig. 4b, similar to the excitatory postsynaptic current by releasing excitatory neurotransmitters. Similarly, the EPSC experiences an extremely slow decay after removing the displacement spike, resulting in long-term potential (LTP) behavior in artificial synapses. Due to large PSC change, denoting the wide modulation range of channel conductance, our TENG-driven synaptic transistor demonstrates a high efficiency in terms of neuromorphic computing. To further exploit the influence of stimuli amplitude, we further investigate the spike-amplitude-dependent plasticity (SADP) by adopting different displacements as the presynaptic action potentials with 10 s interval. As the mechanical displacement increases from 10 to 30 μm with 0.2 s duration, the value of IPSC exhibits a stepwise decreasing behavior from 15 nA to 50 pA, introducing multilevel states of

the synaptic weight, as shown in Fig. 4c. We executed a programming operation by applying positive triboelectric potential before characterizing the EPSC. Analogously, consecutive displacement exhibitory synaptic potentials denoted as the increased displacement from −10 to −30 μm (duration time at 0.2 s, interval time at 10 s) in the opposite direction, the EPSC value increases from 0.5 pA to 6 nA and maintains steadily at each current level (Fig. 4d). To better understand how temporal information of single mechanical displacement can affect the synaptic response, we also demonstrate the spike-time-dependent plasticity (SDDP), which can be evaluated by the synaptic weight. Fig. 4e shows the response of the IPSC to different *D* duration time with the same amplitude of 12 μm. By increasing the spike duration of the separation state from 0.2 to 3 s, the IPSC decreases from 2 to 0.9 nA. The greatly lower conductance state suggests that longer duration is normally sufficient to induce more and more electrons trapped in the graphene layer to modulate WSe_2 channel conductance and leads to a lower current amplitude. The calculated synaptic weight (*Δ*PSC/PSC) increases from 48% to 90%, followed by the saturation, exhibiting continually variable connection strength. The response of EPSC also shows a much more remarkable increment trend from 11.7 to 58 nA with displacement (−30 μm) of pulse width ranging from 0.2 to 3 s. Likewise, the extracted synaptic weight shows an increment trend from 225% to 1605%. Moreover, the energy consumption per spike can be significantly reduced to 74.2 fJ with a small drain voltage of −100 mV (Fig. S10 online), which is analogous to a human synapse (1–100 fJ). As the triboelectric potential derived from mechanical displacement can completely replace the gate supply to power the artificial synapses in a self-powered fashion [40, 41]. No additional power supply is required for TENG. The displacement pulses of TENG can serve as the presynaptic inputs to trigger the PSC without extra presynaptic spike voltage. This design results in removing the capacitive charging energy and reducing total energy consumption. Furthermore, the comparisons of the synaptic weight and the energy consumption are given in Table S1 (online), which shows the extended synaptic weight and ultra-low energy consumption of our artificial synapse. The proposed mechanoplastic synaptic transistor provides the possibility of simulating energy-efficient neuromorphic computing systems. Notably, we realize excellent facilitation and depression characteristics, long-term memory

behavior parallel with ultra-low consumption of the neuromorphic transistor through the integration of TENG component, illustrating good consistency with biological synapses.

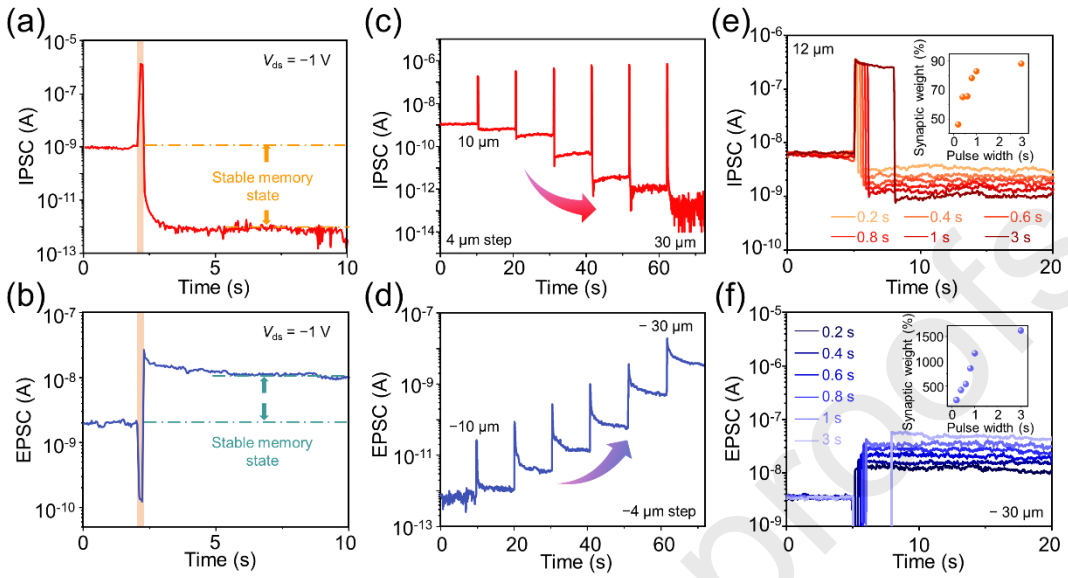

Fig. 4. (Color online) The fundamental synaptic features of the SFG-FET device for single displacement pulse response. (a) Instantaneous IPSC triggered by a positive displacement spike (30 μm, 0.2 s). (b) Instantaneous EPSC triggered by a negative displacement spike (−18 μm, 0.2 s). (c) The IPSC in response to multiple continuous *D* amplitudes from 10 to 30 μm with 0.2 s duration and 10 s interval. (d) The EPSC in response to multiple continuous *D* amplitudes from −10 to −30 μm with 0.2 s duration and 10 s interval, confirming the modulated multilevel states as synaptic weights. (e) The IPSC responses under different *D* duration time from 0.2 to 3 s. (f) The EPSC responses under different *D* duration time from 0.2 to 3 s. Inset of (e) and (f): extracted synaptic weight (*Δ*PSC/PSC) versus *D* pulse width.

3.5. Advanced synaptic features of the mechanoplastic artificial synapse

In mimicking the short-term plasticity features of biological neural systems, paired-pulse-facilitation (PPF) and paired-pulse-depression (PPD) are regarded as critical parameters for temporal information decoding [42]. A schematic diagram of biological and artificial synapse is illustrated in Fig. 5a, which highlights signal information between pre-synapse and post-synapse triggered by a pair of electrical pulses and mechanical pulses respectively. When evoked by two successive and identical presynaptic synapses, the amplitude of PSC triggered by the second spike is larger/smaller appreciably than that by the first spike, referred to as

PPF/PPD. The PPF and PPD behaviors are emulated by applying a pair of displacement spikes (D = ± 30 μm, t = 0.2 s) with a time interval (Δt) of 0.2 s. The left part in Fig. 5b shows the PPD behavior, defined as the relative amplitude (A) triggered by the second D spike, is subject to stronger inhibition. Moreover, the right part in Fig. 5b shows the PPF behavior, corresponding to the phenomenon that the relative amplitude is larger for the second D spike. Also, The PPD index is defined as the ratio of the magnitude of the second PSC (A_2) to the first PSC (A_1) to quantify the facilitation degree of the artificial synapses. The variation of PPD index as a function of the TENG displacement elucidates a decreasing trend of the PPD with larger successive displacements (Fig. 5c). The PPD value peaks at 198% when D = 4 μm and eventually approaches 100% when D = 12 μm. Such a trend manifests that the number of tunneling charges is more susceptible to the first displacement spike and thus the depression quality will be weakened with the action of larger paired displacement pulses. The result mentioned in Fig. 4c verifies that a larger displacement spike can effectively trigger a smaller absolute value of IPSC. Nevertheless, the PPD index mainly reflects relative change under the stimulus of paired displacement spikes, associated with triboelectric potential induced carriers. At the end of the first positive displacement pulse, large numbers of electrons are induced to the tunnel and residue in the graphene layer. If continuing to implement the second displacement pulse closely after a short time interval (0.2 s), there is a limit amount to the tunneling electron since the presence of electrons in the floating layer, thus leading to the lower PPD index. Fig. 5d and Fig. S11a (online) show respectively the LTP and LTD characteristics under a series of negative and positive relative displacement pulses with the same pulse width of 0.2 s. After applying 50 multiple consecutive D pulses with 0.2 s interval and a reading voltage of −1 V, the EPSC exhibits a gradual increment trend with more displacement pulses, where the value of IPSC gradually decreases as the number of TENG spike increases. We take D = −16 and 2 μm as an example to show the evoked gain value, expressed as A_n/A_1, where A is the amplitude of PSC (Fig. 5e). Both the EPSC and IPSC gain exhibit a significant trend, increasing from 34 to 530 and from 4 to 10. The obvious differences between the two gains may be attributed to the fact that the initial EPSC (≈10^{-12} A) is easily triggered by a single displacement spike and improves directly to a high level. Hence, the subsequent pulses have a more obvious impact on the EPSC value. Under the imposition

of small consecutive displacements at $D = -18$ and -22 μm, the current gains increase with the increase of spike numbers, that is, enhanced potential effect. The potential gain values decrease with increased D amplitudes and eventually tend to a state with little variation under large displacements at $D = -30$ μm (Fig. 5f), proving that the larger multiple displacement pulses determine the finite amount of tunneling carrier and hence have a trivial impact on the current ratio. The similar pattern agrees well with the exhibitory behavior illustrated in Fig. S11b (online). To emulate the transition from short-term memory (STM) to long-term memory (LTM), various numbers of D pulse (n = 5, 10, and 50) with the same duration of 0.2 s as stimuli to trigger PSCs (Fig. 5g). The changes of current level are measured at a fixed drain voltage of −1 V. After applying multiple D pulses (n = 5), the evoked EPSC rapidly drops from 47.4 to 14.6 pA in a short time period of 10 s, indicating the STM behavior. The PSC shows an increment trend with increased spike numbers and the current value can still maintain at a relatively stable level of 1.4 nA after about 500 s at n = 50, attesting to the LTM behavior (the inset of Fig. 5g). Learning-experience behavior can also be realized by using two sequences of consecutive D pulses as shown in Fig. 5h. When the device is triggered by the first 20 consecutive D pulses, the EPSC increases gradually, corresponding to a learning process. After removing the pulse train, the spontaneous decay of EPSC within 120 s implies the subsequent forgetting of partial information. For the second learning stage, 6D pulses are enough to achieve the same current level, which is similar to the relearning process in the human brain. It seems to be easier to relearn the forgotten information than the first time, confirming the feasibility of the imitative learning-forgetting-relearning process in our synapse devices analogy to the scenario where the information remains in the cerebral cortex after iterative learning in biological systems [43].

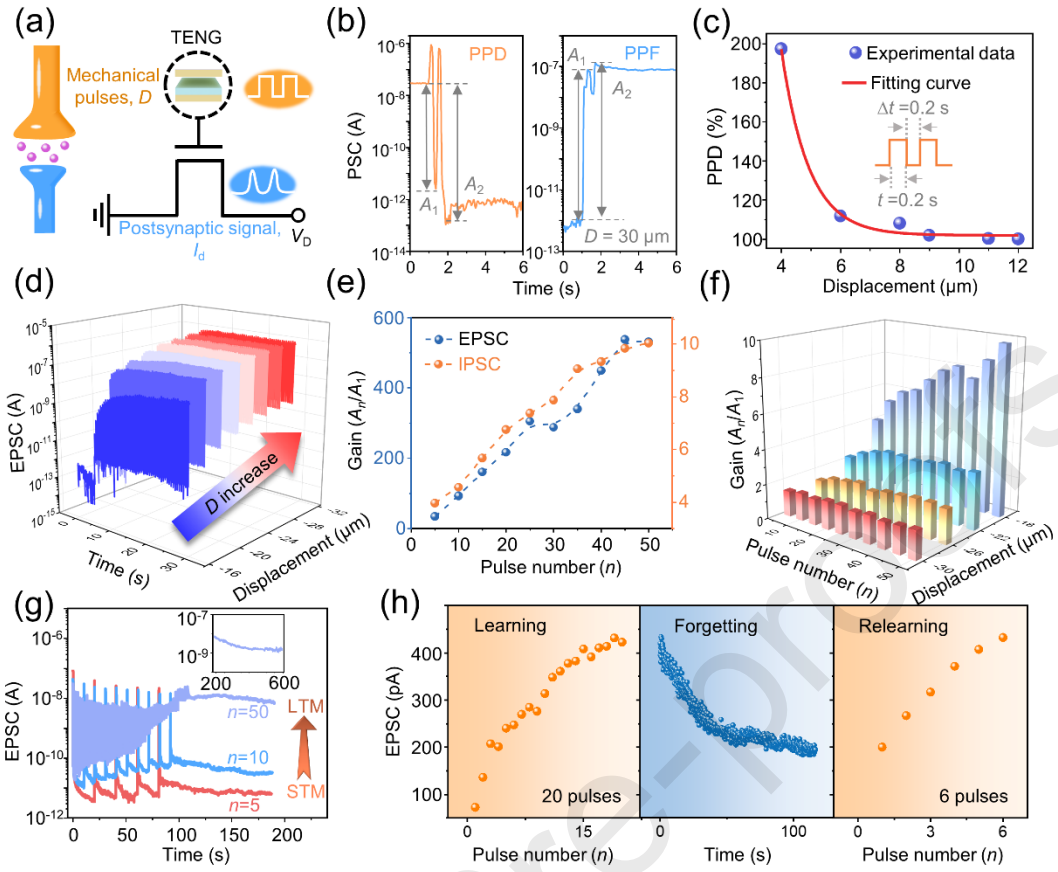

Fig. 5. (Color online) The synaptic plasticity of the TENG-driven SFG-FET devices. (a) Schematic illustration of a biological synapse and artificial synapse by mechanical displacement pulse showing signal information process. The mechanical pulses derived from TENG act as the input spike. (b) PPD and PPF behaviors showing PSC change triggered by two consecutive displacement pulses (D = ± 30 μm) with time interval Δt of 0.2 s and pulse width of 0.2 s. A_1 and A_2 are the amplitudes of the first and second PSC peak, respectively. (c) Extracted PPD index (A_2/A_1×100%) versus applied displacement. (d) EPSC dependence on number of displacement pulses with pulse width of 0.2 s, time interval of 0.2 s, and various D amplitudes (from −16 to −30 μm). (e) Calculated gain (A_n/A_1) of EPSC and IPSC response as a function of number of displacement pulse with D = −16 and 2 μm. (f) Gain plotted as a function of pulse number with D at −18, −22, −26, −30 μm. (g) Changes of EPSC after different number of applied D pulses (D amplitude = −24 μm, pulse width = 0.2 s), showing the transition from STM to LTM. (h) Emulation of learning-experience behavior. The EPSC increasing with number of D pulses corresponds to the learning or relearning process, while the EPSC decaying corresponds to the forgetting process.

4. Conclusion

In summary, we have successfully demonstrated a nonvolatile and programmable semifloating-gate transistor based on graphene/h-BN/WSe_2 heterostructure integrated with the TENG component. Under the synergistic effect of triboelectric potential derived from mechanical displacement, the channel conductance exhibits a continuously adjustable behavior by manipulating the type and density of trapped carriers in the floating layer, thus leading to the different working states. Meanwhile, the SFG-FET device exhibits a high on/off current ratio of 10^6, a long retention time of 1200 s, and excellent dynamic switching behavior. The transistor can be readily reconfigured as p-n or n^+-n junctions by integrating mechanical modulation, which paves the way towards the functional customization of versatile and multifunctional electronics. Furthermore, the representative synaptic functions in the biological nervous system such as short-/long-term plasticity have been emulated in our artificial synapse. The synaptic weight can be simply modulated by mechanical displacement, thus endowing the transistor with learning and memory capability. Along with recognizing spatiotemporal information of mechanical stimuli (e.g., amplitude and duration time), the synaptic transistor also enables multilevel data storage capacity, which benefits from large synaptic weight change. Under the synergism of the semifloating layer, the artificial synapse can also realize successive neural facilitation/depression, memory function, and learning-experience behavior. The proposed TENG-driven artificial synapse proves the exciting potential for a direct interaction between mechanical behavior and synaptic plasticity modulation behavior, aiming to build a neuromorphic computing system with high processing efficiency, high integration and low energy consumption.

Conflict of interest

The authors declare that they have no conflict of interest.

Acknowledgments

This work was supported by the National Natural Science Foundation of China (51872031, 52073032, and 61904013) and the Fundamental Research Funds for the Central Universities.

Journal Pre-proofs

Author contributions

Mengmeng Jia and Pengwen Guo conceived the idea and designed the experiment. Zhong Lin Wang and Junyi Zhai guided the project. Mengmeng Jia and Pengwen Guo fabricated the devices and performed the experiment. Mengmeng Jia and Junyi Zhai analyzed the data. Mengmeng Jia drew the figures. Mengmeng Jia, Wei Wang, Aifang Yu, Yufei Zhang, and Junyi Zhai prepared the manuscript. All authors discussed and reviewed the manuscript.

Journal Pre-proofs

References

[1] Fuller EJ, Keene ST, Melianas A, et al. Parallel programming of an ionic floating-gate memory array for scalable neuromorphic computing. Science, 2019, 364: 570-574

[2] Boybat I, Le Gallo M, Nandakumar SR, et al. Neuromorphic computing with multi-memristive synapses. Nat Commun, 2018, 9: 2514

[3] Wong HSP, Salahuddin S. Memory leads the way to better computing. Nat Nanotechnol, 2015, 10: 191-194

[4] Ho VM, Lee J-A, Martin KC. The cell biology of synaptic plasticity. Science, 2011, 334: 623-628

[5] Abbott LF, Regehr WG. Synaptic computation. Nature, 2004, 431: 796-803

[6] Kim Y, Chortos A, Xu W, et al. A bioinspired flexible organic artificial afferent nerve. Science, 2018, 360: 998-1003

[7] Jiang J, Guo J, Wan X, et al. 2D MoS_2 neuromorphic devices for brain-like computational systems. Small, 2017, 13: 1700933

[8] John RA, Liu F, Nguyen Anh C, et al. Synergistic gating of electro-iono-photoactive 2D chalcogenide neuristors: coexistence of hebbian and homeostatic synaptic metaplasticity. Adv Mater, 2018, 30: 1800220

[9] Ielmini D, Wong HSP. In-memory computing with resistive switching devices. Nat Electron, 2018, 1: 333-343

[10] Wang Z, Joshi S, Savel'ev SE, et al. Memristors with diffusive dynamics as synaptic emulators for neuromorphic computing. Nat Mater, 2017, 16: 101-108

[11] Wang H, Zhao Q, Ni Z, et al. A ferroelectric/electrochemical modulated organic synapse for ultraflexible, artificial visual-perception system. Adv Mater, 2018, 30: 1803961

[12] Tian H, Mi W, Wang XF, et al. Graphene dynamic synapse with modulatable plasticity. Nano Lett, 2015, 15: 8013-8019

[13] Zhu J, Yang Y, Jia R, et al. Ion gated synaptic transistors based on 2D van der Waals crystals with tunable diffusive dynamics. Adv Mater, 2018, 30: 1800195

[14] Ni Y, Ma M, Wei H, et al. Multiplexed neurotransmission emulated for emotion control. Nano Energy, 2021, 86: 106038

[15] Molina-Lopez F, Gao TZ, Kraft U, et al. Inkjet-printed stretchable and low voltage synaptic transistor array. Nat Commun, 2019, 10: 2676

[16] Li E, Wu X, Chen Q, et al. Nanoscale channel organic ferroelectric synaptic transistor array for high recognition accuracy neuromorphic computing. Nano Energy, 2021, 85: 106010

[17] Kim S, Choi B, Lim M, et al. Pattern recognition using carbon nanotube synaptic transistors with an adjustable weight update protocol. ACS Nano, 2017, 11: 2814-2822

[18] Fan F, Tian Z, Wang ZL. Flexible triboelectric generator! Nano Energy, 2012, 1: 328-334

[19] Fan F, Tang W, Wang ZL. Flexible nanogenerators for energy harvesting and self-powered electronics. Adv Mater, 2016, 28: 4283-4305

[20] Fan F, Lin L, Zhu G, et al. Transparent triboelectric nanogenerators and self-powered pressure sensors based on micropatterned plastic films. Nano Lett, 2012, 12: 3109-3114

[21] Wang ZL. Triboelectric nanogenerators as new energy technology for self-powered systems and as active mechanical and chemical sensors. ACS Nano, 2013, 7: 9533-9557

[22] Chen J, Zhu G, Yang J, et al. Personalized keystroke dynamics for self-powered human-machine interfacing. ACS Nano, 2015, 9: 105-116

[23] Pu X, Liu M, Chen X, et al. Ultrastretchable, transparent triboelectric nanogenerator as electronic skin for biomechanical energy harvesting and tactile sensing. Sci Adv, 2017, 3: e1700015

[24] Wang X, Niu S, Yin Y, et al. Triboelectric nanogenerator based on fully enclosed rolling spherical structure for harvesting low-frequency water wave energy. Adv Energy Mater, 2015, 5: 1501467

[25] Wang ZL. New wave power. Nature, 2017, 542: 159-160

[26] Zhang C, Zhang LM, Tang W, et al. Tribotronic logic circuits and basic operations. Adv Mater, 2015, 27: 3533-3540

[27] Sun M, Xie D, Sun Y, et al. Lateral multilayer/monolayer MoS_2 heterojunction for high performance photodetector applications. Sci Rep, 2017, 7: 4505

[28] Xu Z-Q, Zhang Y, Wang Z, et al. Atomically thin lateral p-n junction photodetector with large effective detection area. 2D Mater, 2016, 3: 041001

Journal Pre-proofs

[29] Choi MS, Qu D, Lee D, et al. Lateral MoS_2 p-n junction formed by chemical doping for use in high-performance optoelectronics. ACS Nano, 2014, 8: 9332-9340

[30] Gong Y, Yuan H, Wu C-L, et al. Spatially controlled doping of two-dimensional SnS_2 through intercalation for electronics. Nat Nanotechnol, 2018, 13: 294-299

[31] Ross JS, Klement P, Jones AM, et al. Electrically tunable excitonic light-emitting diodes based on monolayer WSe_2 p-n junctions. Nat Nanotechnol, 2014, 9: 268-272

[32] Baugher BWH, Churchill HOH, Yang Y, et al. Optoelectronic devices based on electrically tunable p-n diodes in a monolayer dichalcogenide. Nat Nanotechnol, 2014, 9: 262-267

[33] Pospischil A, Furchi MM, Mueller T. Solar-energy conversion and light emission in an atomic monolayer p-n diode. Nat Nanotechnol, 2014, 9: 257-261

[34] Lv L, Zhuge F, Xie F, et al. Reconfigurable two-dimensional optoelectronic devices enabled by local ferroelectric polarization. Nat Commun, 2019, 10: 3331

[35] Wu G, Tian B, Liu L, et al. Programmable transition metal dichalcogenide homojunctions controlled by nonvolatile ferroelectric domains. Nat Electron, 2020, 3: 43-50

[36] Gottschaldt KM, Vahlehinz C. Merkel cell receptors: structure and transducer function. Science, 1981, 214: 183-186

[37] Maksimovic S, Nakatani M, Baba Y, et al. Epidermal merkel cells are mechanosensory cells that tune mammalian touch receptors. Nature, 2014, 509: 617-621

[38] Corro Ed, Terrones H, Elias A, et al. Excited excitonic states in 1L, 2L, 3L, and bulk WSe_2 observed by resonant raman spectroscopy. ACS Nano, 2014, 8: 9629-9635

[39] Li D, Chen M, Sun Z, et al. Two-dimensional non-volatile programmable p-n junctions. Nat Nanotechnol, 2017, 12: 901-906

[40] Yu J, Gao G, Huang J, et al. Contact-electrification-activated artificial afferents at femtojoule energy. Nat Commun, 2021, 12: 1581

[41] Liu Y, Zhong J, Li E, et al. Self-powered artificial synapses actuated by triboelectric nanogenerator. Nano Energy, 2019, 60: 377-384

[42] Atluri PP, Regehr WG. Determinants of the time course of facilitation at the granule cell to purkinje cell synapse. J Neurosci, 1996, 16: 5661-5671

[43] Wang ZQ, Xu HY, Li XH, et al. Synaptic learning and memory functions achieved using oxygen ion migration/diffusion in an amorphous InGaZnO memristor. Adv Funct Mater, 2012, 22: 2759-2765

Mengmeng Jia received her B.E. degree in Material Chemistry from Nanjing University of Science and Technology in 2016. Now she is a Ph.D. candidate at the Beijing Institute of Nanoenergy and Nanosystems, Chinese Academy of Sciences. Her research interest is focused on MoS_2-based devices and the tribotronic effect.

Pengwen Guo received his B.E. degree at the School of Materials Science and Engineering, University of Science and Technology Beijing in 2017. He is currently pursuing his Ph.D. degree at Beijing Institute of Nanoenergy and Nanosystems, Chinese Academy of Sciences. His research interest includes flexoelectronics and 2D semiconductors.

Junyi Zhai received his Ph.D. degree from Virginia Polytechnic Institute and State University in 2009. Now he is a professor at Beijing Institute of Nanoenergy and

Journal Pre-proofs

Nanosystems, Chinese Academy of Sciences. His main research interest includes micro/nano piezoelectric semiconductors, sensors and self-power systems.

Zhong Lin Wang is the Chief Scientist and Director of Beijing Institute of Nanoenergy and Nanosystems, Chinese Academy of Sciences. He is also the Regents' Professor and Engineering Distinguished Professor at Georgia Institute of Technology. His research focuses on developing nanogenerators for harvesting mechanical energy from environmental for powering personal electronics, and the field of piezotronics and piezo-phototronics by introducing piezoelectric potential-gated charge transport process in fabricating new electronic and optoelectronic devices.

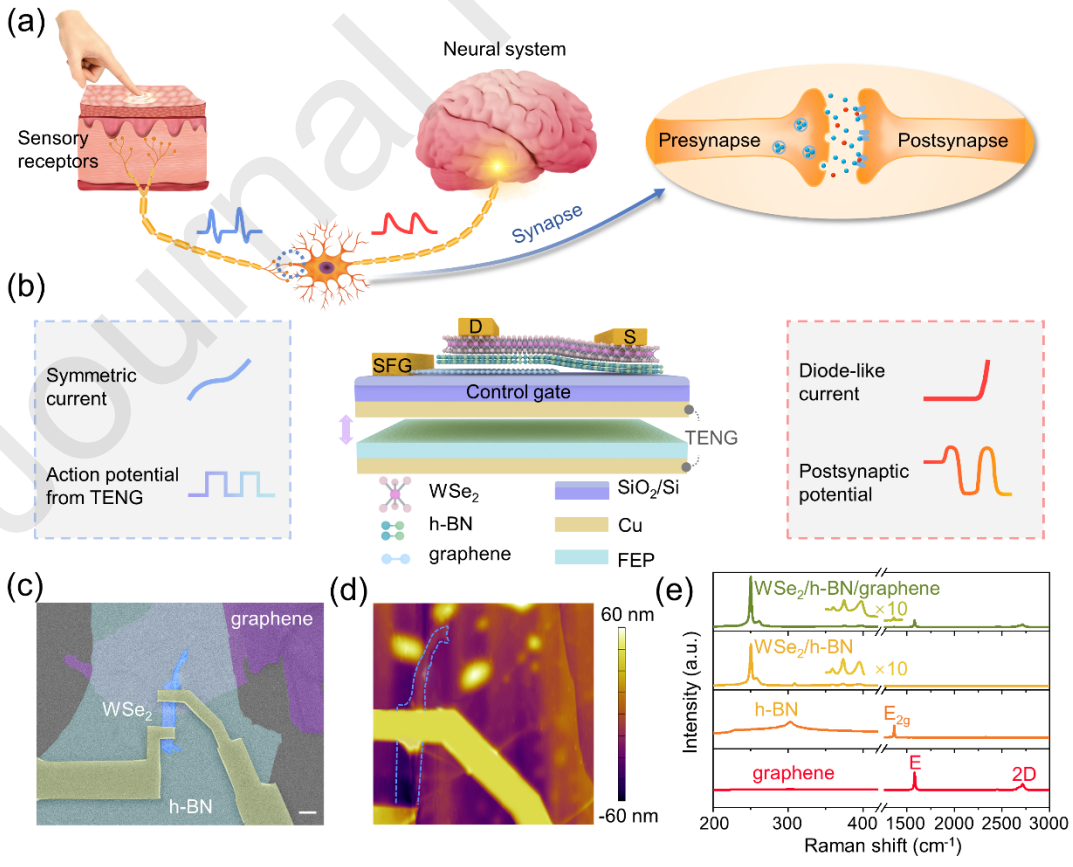

Journal Pre-proofs

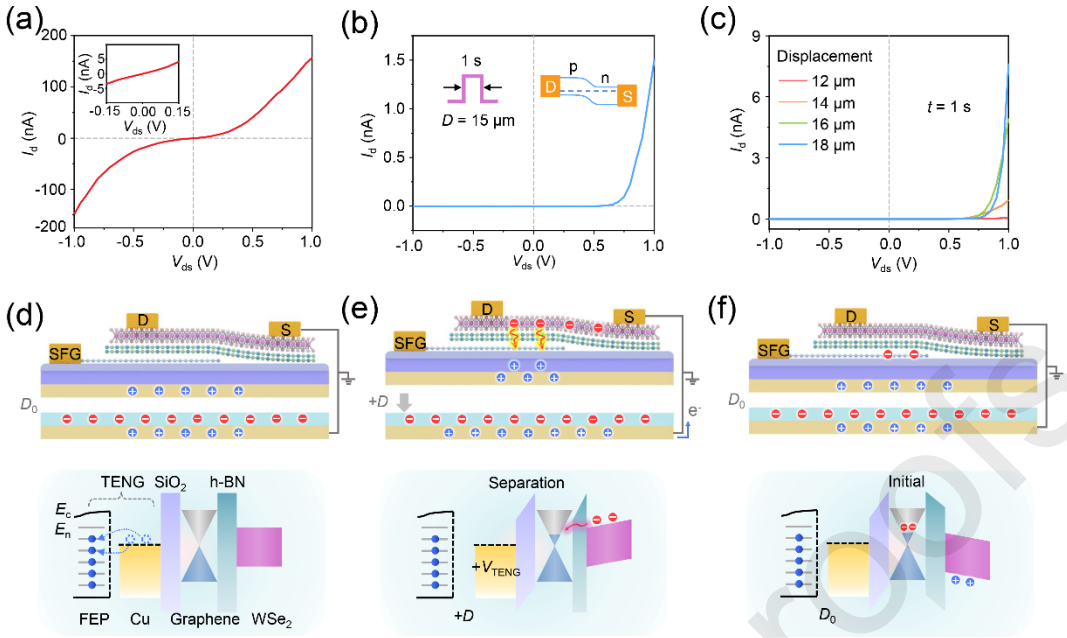

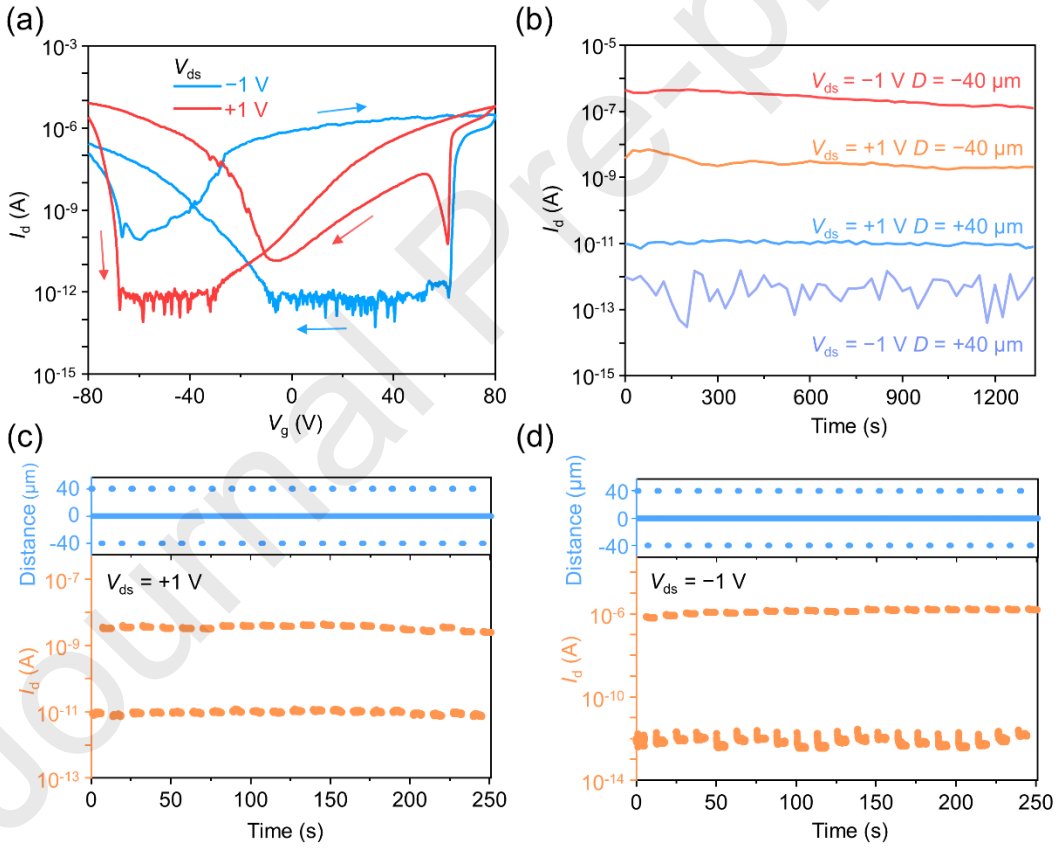

Journal Pre-proofs

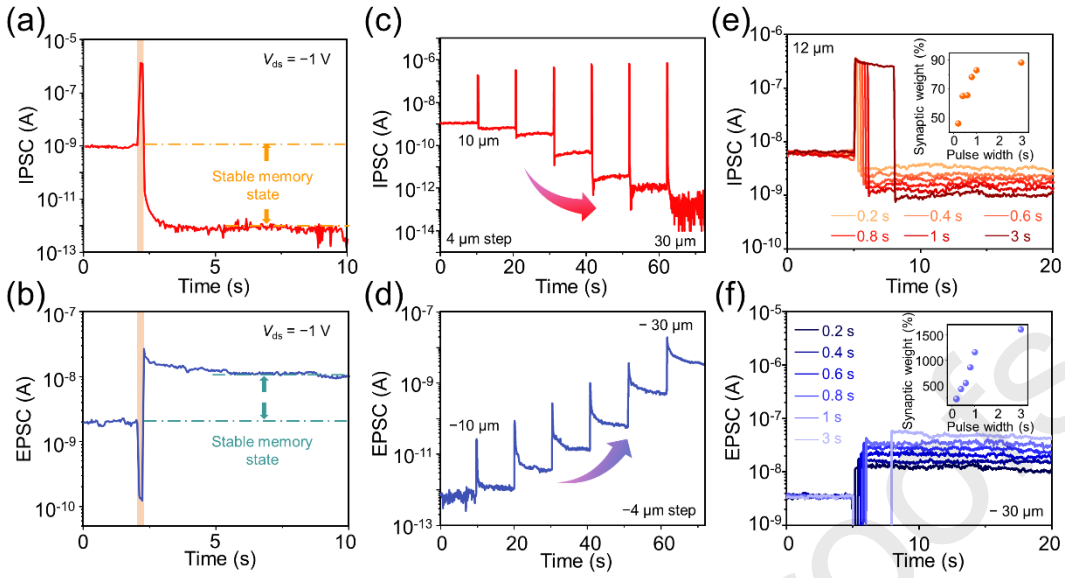

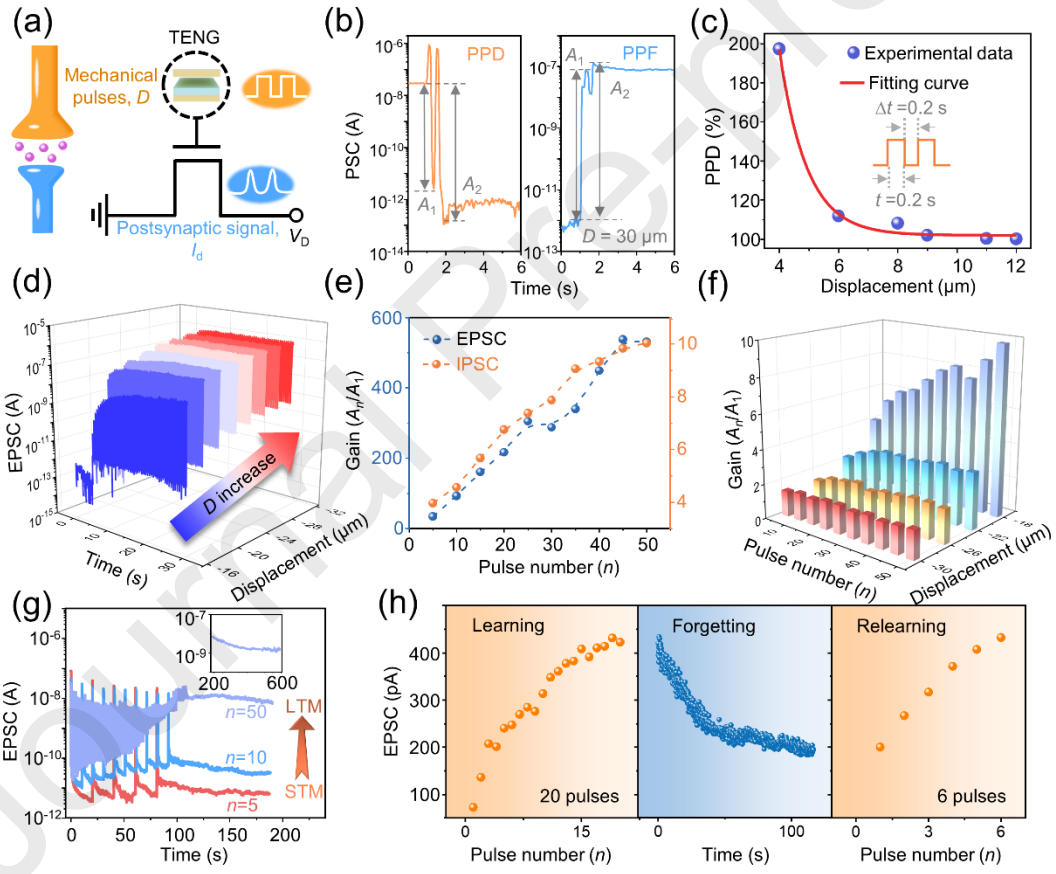

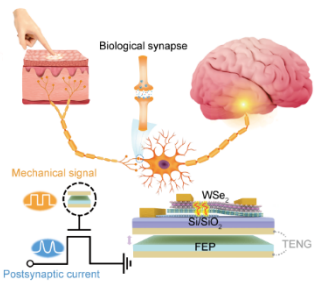

Journal Pre-proofs